ARTICLE

Check for updates

Modulation instability—rogue wave correspondence hidden in integrable systems

Shihua Chen [1,2✉], Lili Bu[1], Changchang Pan[1], Chong Hou[1], Fabio Baronio [3✉], Philippe Grelu [4✉] &
Nail Akhmediev [5✉]

The bulk-boundary correspondence is a key feature of topological physics and is universally applicable to Hermitian and non-Hermitian systems. Here, we report a similar universal correspondence intended for the rogue waves in integrable systems, by establishing the relationship between the fundamental rogue wave solutions of integrable models and the baseband modulation instability of continuous-wave backgrounds. We employ an *N*-component generalized nonlinear Schrödinger equation framework to exemplify this modulation instability-rogue wave correspondence, where we numerically confirm the excitation of three coexisting Peregrine solitons from a turbulent wave field, as predicted by the modulation instability analysis. The universality of such modulation instability-rogue wave correspondence has been corroborated using various integrable models, thereby offering an alternative way of obtaining exact rogue wave solutions from the modulation instability analysis.

[1] School of Physics and Frontiers Science Center for Mobile Information Communication and Security, Southeast University, Nanjing 211189, China. [2] Purple Mountain Laboratories, Nanjing 211111, China. [3] Consorzio Nazionale Interuniversitario per le Telecomunicazioni and Dipartimento di Ingegneria dell'Informazione, Università di Brescia, Via Branze 38, 25123 Brescia, Italy. [4] Laboratoire ICB, U.M.R. 6303 C.N.R.S., Université Bourgogne Franche-Comté, 9 avenue A. Savary, F-21078 Dijon, France. [5] Department of Fundamental and Theoretical Physics, Research School of Physics, The Australian National University, Canberra, ACT 2600, Australia. ✉email: cshua@seu.edu.cn; fabio.baronio@unibs.it; philippe.grelu@u-bourgogne.fr; nail.akhmediev@anu.edu.au

Rogue waves are a broad multidisciplinary subject of research with areas spanning from oceanography[1] to hydrodynamics[2,3], optics and photonics[4–6], acoustics[7], Bose-Einstein condensation[8], and artificial intelligence[9,10]. From a microscopic perspective, they can be referred to as a class of deterministic rational solutions of the integrable nonlinear partial differential equations, which entail a doubly-localized peak on a finite background[11,12]. The well-known Peregrine soliton is an example of such deterministic rational solutions[13], which provides an appealing paradigm to confront the mystique surrounding realistic rogue waves[14–19]. So far, Peregrine soliton events have been experimentally observed in such physical settings as the water-wave tank[2], deep-water flumes[3], optical fibres[20], plasmas[21], and irregular oceanic sea states[22].

The relation of rogue wave states to integrable systems can be virtually reminiscent of that of the topological edge modes to Hermitian systems[23,24]. For instance, rogue wave states are exact solutions of the integrable models obtained with inverse scattering transform[25] or Darboux transformation[12], while gapless edge modes can be analytically obtained by solving the eigenproblem of Hermitian Hamiltonian[26,27]. Although rogue waves and topological edge modes are two different wave localization phenomena, both of them are immune to perturbations (more precisely, the former always come with perturbations[17], while the latter are topologically protected against perturbations[28]), and can exist for a broad range of system parameters[24]. Further, it has been demonstrated, both theoretically and experimentally, that rogue waves are seen in either integrable[2,11,15] or non-integrable[4,5,29] systems as often as the topological edge modes are in either Hermitian[23,24] or non-Hermitian[27,30] systems. Interestingly, a direct application of topological concept into rogue wave phenomena so as to realize topological control of extreme waves has also been recently reported[31]. As is well known, the basic principle behind the topological edge modes is the bulk-boundary correspondence[32,33], which relates the robust edge states to the topological invariants of the bulk[34–36]. Now a natural question arises: What is the genuine mechanism underlying the rogue wave formation? Or equivalently, is there a similar correspondence principle intended for the rogue waves in integrable systems? An affirmative answer to this question will be provided in this paper.

In fact, there have been intense research activities on the mechanisms or physics behind the rogue wave events in the past decade. Numerous studies[37–46] show that a possible mechanism for such rogue formation is the modulation instability (MI) (sometimes called Benjamin-Feir instability[47]), which traces the growth of periodic perturbations on an unstable continuous-wave (cw) background seeded by noises. In the initial stage of MI, the spectral sidebands associated with the instability undergo exponential growth, but subsequently a dramatic energy exchange may occur among multiple spectral modes, resulting in a series of high-contrast peaks of random intensity where Peregrine soliton structures can be identified[12,17]. In addition to MI, there are also emerging several other explanations for rogue wave generation, e.g., integrable turbulence[48,49], breather or soliton collisions[50–52], random superposition of Stokes waves[53], and the spatial asymmetry or inhomogeneity[54,55]. These investigations provide a good perspective on the fundamental origin of rogue waves, but how to clarify such a controversial issue is still an open challenge of this emerging field.

In this work, we unveil, on an analytic level, a direct kinship between the baseband MI[39] of cw backgrounds and the rogue wave solutions of integrable models, which goes beyond the prediction of the domains of existence for rogue waves[12,40]. Here, by baseband MI we mean the instability experienced by the cw background in a region where the perturbations feature infinitesimally small frequencies[12]. Such MI-rogue wave correspondence is an analog of the bulk-boundary correspondence in topological physics, with rogue waves corresponding to the boundary modes and MI corresponding to the bulk topological invariant, respectively. It applies universally to almost all integrable systems, even to those whose rogue wave solutions can not be expressed in terms of elementary functions. To support the universal scope of our results, we consider a model of N-component generalized nonlinear Schrödinger (GNLS) equation, which includes the celebrated NLS[56] and Manakov[57–59] models as well as their N-component versions[60–62] as special cases. Within this framework, we establish the one-to-one correspondence between the rogue wave solutions and the MI baseband spectra, and numerically confirm it by demonstrating the excitation of three coexisting Peregrine solitons from a turbulent wave field[63] for the specific $N = 3$ case. Meanwhile, the universality of this MI-rogue wave correspondence has been corroborated with various integrable models. As is expected, aside from offering a way of obtaining exact rogue wave solutions from the MI analysis, our work unequivocally substantiates the insight that MI is the most fundamental mechanism underlying the rogue wave formation.

Results and discussion

GNLS model and MI evolution equation. For our studies, we write the N-component GNLS model in dimensionless form

$$\mathrm{i}\frac{\partial u_j}{\partial z} + \frac{\sigma}{2}\frac{\partial^2 u_j}{\partial t^2} + \left(\sum_{m=1}^{N}|u_m|^2\right)\left(u_j + \mathrm{i}\gamma\frac{\partial u_j}{\partial t}\right) = 0, \qquad (1)$$

where $j = 1,..., N$ and $u_j(z, t)$ is the normalized complex envelope of the jth-component wave field, with z and t the independent variables. The real parameter σ represents the type of dispersion, i.e., the anomalous dispersion for $\sigma > 0$ and the normal dispersion for $\sigma < 0$. The third term combines the self- and cross-phase modulation effect, whose coefficient has been normalized to unity, and the self-steepening effect defined by the parameter γ[64,65]. In quadratic nonlinear media, the self-steepening seen by ultrashort pulses is controllable in both sign and magnitude and thus provides a new degree of freedom wherever shock formation is significant[66–68]. We should emphasize that the multiple-component model (1) is of considerable physical interest not only because it includes the celebrated NLS[56] and Manakov[57–59] models as well as their integrable extensions[46,69–71], but also because it itself ($N \geqslant 3$) may find applications in such fields as wavelength division multiplexing[72], Bose-Einstein condensation[73], and Davydov solitons in biophysics[74]. More fundamentally, the model (1) owns complete integrability (also known as complete solvability)[75] and all complicated rogue wave signatures known so far[46], and is therefore appropriate for investigating the intriguing MI-rogue wave correspondence.

Let us first derive the MI evolution equation based on the plane-wave solutions of Eqs. (1),

$$u_{j0} = a_j \exp(\mathrm{i}\omega_j t - \mathrm{i}k_j z), \quad j = 1,\cdots,N, \qquad (2)$$

where the amplitudes $a_j \in \mathbb{R}$, the wavenumbers $k_j \in \mathbb{R}$, and the frequencies $\omega_j \in \mathbb{R}$ obey the dispersion relations:

$$k_j = Av_j + \frac{1}{2}\sigma\omega_j^2, \quad v_j = \gamma\omega_j - 1, \qquad (3)$$

with $A = \sum_{j=1}^{N} a_j^2$ being the sum of background intensities. Then, we add the small amplitude Fourier modes associated with r_j and w_j ($j = 1,...,N$) to the plane-wave solutions (2) and express them as

$$u_j = u_{j0}\{1 + r_j \exp[\mathrm{i}\Omega(\kappa z + t)] + w_j^* \exp[-\mathrm{i}\Omega(\kappa^* z + t)]\}, \qquad (4)$$

where $\Omega \in \mathbb{R}$ denotes the frequency offset from the central frequencies ω_j, $\varkappa$ is a complex wavenumber induced by perturbations, and the asterisk means complex conjugate. When these perturbed plane-wave solutions are substituted into Eqs. (1), followed by linearization, a system of $2N$ coupled linear equations about r_j and w_j can be obtained, which will have a nontrivial solution only when $\wp = (\varkappa + A\gamma)/\sigma$ satisfies the dispersion relation (see Supplementary Note 1 for details):

$$\sum_{j=1}^{N} \frac{a_j^2 v_j}{(\wp + \omega_j)^2 - \Omega^2/4} = \sigma. \tag{5}$$

It is seen that only if $\varkappa$ or $\wp$ is a complex number does the MI occur. Therefore, we define the MI gain as $\gamma_h = |\Omega\Im(\varkappa)| = |\sigma\Omega\Im(\wp)|$, where the symbol $\Im$ means taking the imaginary part[12]. It should be noted that the MI evolution Eq. (5) depicts the instability of the cw backgrounds, not that of the solitons or other localized entities allowed.

Closed-form Peregrine soliton solutions. On the other hand, thanks to integrability, the GNLS model (1) can be solved by means of Darboux transformation[46,76,77] or the Hirota bilinear method[61,78]. Its general fundamental rogue wave solutions are expressed as, in an elegant closed form

$$u_j = u_{j0}\left(1 + \frac{iG_j}{M}\right), \quad j = 1, \cdots, N, \tag{6}$$

where the polynomials M and G_j are defined by

$$M = \tau^2 + \sigma^2 v^2 z^2 + \frac{\eta^2}{4\alpha v^2} - \frac{i\gamma}{\alpha}(\sigma\gamma v^2 z - \eta\tau), \tag{7}$$

$$G_j = \frac{2\left[(\mu + \omega_j)\tau - \sigma v^2 z\right]}{(\mu + \omega_j)^2 + v^2} + \frac{2\gamma(\sigma\gamma v^2 z - \eta\tau)}{\alpha} - \frac{i\eta v_j}{\alpha\left[(\mu + \omega_j)^2 + v^2\right]}, \tag{8}$$

with $\tau = t + (\sigma\mu - \gamma A)z$, $\eta = \gamma\mu + 1$, and $\alpha = \gamma^2 v^2 + \eta^2$. Here, the parameters $\mu \in \mathbb{R}$ and $v \in \mathbb{R}$ are the real and imaginary parts of the complex root $\wp = \mu + iv$ of the $2N$-degree polynomial equation:

$$\sum_{j=1}^{N} \frac{a_j^2 v_j}{(\wp + \omega_j)^2} = \sigma. \tag{9}$$

We should point out that when $N = 1$, such fundamental rogue wave solutions has been presented in ref. [71], and when $N = 2$, they have just recently been reported in ref. [46], all obtained with the Darboux transformation method.

We should point out that the closed-form solutions (6) can reveal all forms of Peregrine soliton structures that are allowed by the GNLS model (1), including those that can not be expressed in terms of elementary functions, which always occur for $N \geqslant 3$ (see Supplementary Note 2). Therefore, for the latter circumstances, one needs to first solve the characteristic polynomial Eq. (9) numerically for μ and v, which can easily be done by commercial analytic tools. Then, the exactitude of the solutions (6) can be well confirmed.

As one can see, the characteristic Eq. (9) is none other than the MI evolution Eq. (5) in the baseband limit $\Omega = 0$, although they are derived in a different way. This implies that there is a direct one-to-one relationship between the baseband MI and the rogue wave solutions, namely, for every complex root $\wp = \mu + iv$ ($v \neq 0$) of Eq. (5) obtained with $\Omega = 0$, the rogue wave solutions (6) are uniquely determined, and if more pairs of complex $\wp$ exist, more rogue wave states are allowed to occur. This is what we called MI-

rogue wave correspondence, which is a universal principle hidden in integrable nonlinear equations not limited to the GNLS model (1). In our Methods or Supplementary Note 3, we also demonstrate its validity in the context of other integrable models.

MI-rogue wave correspondence and exemplification. Subsequently, to exemplify this interesting MI-rogue wave correspondence, we examine below the three-component case ($N = 3$) without loss of generality. In this situation, one needs to solve Eq. (5) for $\wp = \mu + iv$ in the baseband limit $\Omega = 0$. Generally, it is a sextic real-coefficient polynomial equation of $\wp$ and only a very few cases do admit the analytic solutions (see Supplementary Note 2). Let us cite here one example of such analytic solutions, where $\omega_3 = (\omega_1 + \omega_2)/2 = \kappa_{12}/2$ is taken. When $\delta_{12} = \omega_1 - \omega_2 = 0$ (i.e., the simple decoupled situation), it is easily found that there is at most one pair of complex roots of $\wp$, given by

$$\mu = -\omega_1, \quad \nu = \sqrt{-A v_1/\sigma}, \quad \text{for } \sigma v_1 < 0. \tag{10}$$

When $\delta_{12} \neq 0$, this sextic equation can still be solved analytically under the amplitude conditions

$$a_1 = \sqrt{-\frac{\sigma\delta_{12}^2}{3v_1}}, \quad a_2 = \sqrt{-\frac{\sigma\delta_{12}^2}{3v_2}}, \quad a_3 = \sqrt{-\frac{\sigma\delta_{12}^2}{3v_3}}, \tag{11}$$

for $\sigma v_{1,2,3} < 0$, yielding three pairs of complex roots:

$$\text{(I)} \, \mu = -\frac{\kappa_{12}}{2}, \quad \nu = \frac{\sqrt{3}}{6}|\delta_{12}|\left(\bar{\omega}^2 + \frac{1}{\bar{\omega}^2}\right), \tag{12}$$

$$\text{(II)} \, \mu = \frac{\delta_{12}}{4}\left(\bar{\omega}^2 - \frac{1}{\bar{\omega}^2}\right) - \frac{\kappa_{12}}{2}, \quad \nu = \frac{\sqrt{3}}{12}|\delta_{12}|\left(\bar{\omega}^2 + \frac{1}{\bar{\omega}^2}\right), \tag{13}$$

$$\text{(III)} \, \mu = -\frac{\delta_{12}}{4}\left(\bar{\omega}^2 - \frac{1}{\bar{\omega}^2}\right) - \frac{\kappa_{12}}{2}, \quad \nu = \frac{\sqrt{3}}{12}|\delta_{12}|\left(\bar{\omega}^2 + \frac{1}{\bar{\omega}^2}\right), \tag{14}$$

where $\bar{\omega} = (\sqrt{2} + 1)^{1/3} \approx 1.3415$. It should be noted that we have dropped the $\pm$ sign from the above v formulas, as the rogue wave solutions depend on v^2 only.

Figure 1 a–c displays the landscapes of the positive imaginary parts of $\wp$ versus ω_1 and ω_2 in the baseband limit ($\Omega = 0$), obtained numerically using a typical set of initial parameters $\sigma = -1$ (normal dispersion), $\gamma = 1$, $a_1 \simeq 1.1656$, $a_2 \simeq 0.5693$, $a_3 \simeq 0.7234$, and letting $\omega_3 = (\omega_1 + \omega_2)/2$. The cross-sectional profiles $\Im(\wp_j)$ with respect to ω_1 or ω_2 are illustrated in Fig. 1d–f. Since in such a baseband limit, the real and imaginary parts of $\wp$ give the values of μ and v, respectively, these maps clearly reveal the rogue wave signatures in the phase space (ω_1, ω_2). To be specific, as every points beyond the line $\delta_{12} = 0$ are completely covered by these maps (Fig. 1a–c), the solutions (6) can therefore exist in the whole domain of ω_1 and ω_2, apart from some particular points on that line which exclude any rogue wave solutions in both dispersion situations. It is also suggested that in the top right domain defined by $\sigma v_{1,2,3} < 0$ and $\delta_{12} \neq 0$, there would occur three different rogue wave structures for given set of initial parameters (Fig. 1f). In other domains, at most two different structures are allowed, as indicated in Fig. 1d, e. Here we should point out that although two curves of $\Im(\wp) = v$ may coincide at some points in Fig. 1d–f, they still represent two different rogue wave structures since the real parts $\Re(\wp) = \mu$ are now different at these points.

We also calculate numerically $\Im(\wp_j)(\geqslant 0)$ and the corresponding MI gains $\gamma_{hj} = |\sigma\Omega\Im(\wp_j)|$ from Eq. (5) under the same parameter conditions as in Fig. 1, but now allowing Ω to vary.
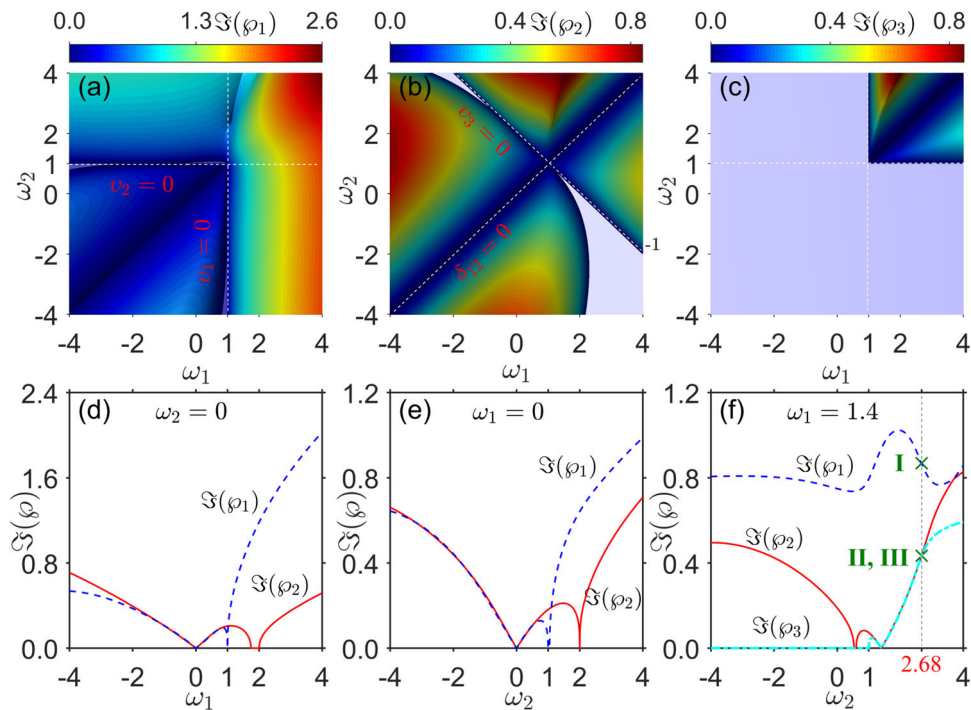
Fig. 1 Landscapes of the positive imaginary parts of $\wp$ in the baseband limit and cross-sectional profiles. a–c Landscapes of $\Im(\wp_j)$ as a function of the frequencies ω_1 and ω_2. Here $\wp_j (j = 1,2,3)$ are the complex roots of Eq. (5) in the baseband limit $\Omega = 0$, with $\wp_3 = (\omega_1 + \omega_2)/2$, and $\Im$ denotes the positive imaginary part of these roots, if any. The other parameters are specified by $\sigma = -1$ (normal dispersion), $\gamma = 1$, $a_1 \simeq 1.1656$, $a_2 \simeq 0.5693$, and $a_3 \simeq 0.7234$. The white dashed lines in **a**, **b**, **c** are auxiliary ones that can separate the maps into different regions and the colour bars on the top quantify the magnitude of $\Im(\wp_j)$. **d–f** Cross-sectional profiles of $\Im(\wp_j)$ with respect to (**d**) ω_1 or (**e**, **f**) ω_2, given the ω_2 or ω_1 value on the top of each panel. Here, the blue dashed line, red solid line, and cyan dash-dotted line represent $\Im(\wp_1)$, $\Im(\wp_2)$, and $\Im(\wp_3)$, respectively. The green crosses in (**f**) indicate the values of $\nu = \Im(\wp)$ for Cases I, II, and III calculated respectively from Eqs. (12), (13), and (14), wherein $\omega_1 = 1.4$ and $\omega_2 \simeq 2.68$.

The results corresponding to $\omega_1 = 0$ (left column) and $\omega_1 = 1.4$ (middle and right columns) are presented in Fig. 2. It is seen that when $\omega_1 = 0$, there exist only two symmetrically distributed imaginary parts $\Im(\wp_{1,2})$ for almost all ω_2 values (Fig. 2a, b), whereas when $\omega_1 = 1.4$, there are three imaginary parts $\Im(\wp_{1,2,3})$ for $\omega_2 > 1$ (Fig. 2c–e). Each $\Im(\wp_j)$ involves a baseband part that traverses the central line $\Omega = 0$, but the main spectrum $\Im(\wp_1)$ is usually more complicated, as it may possess several passbands as well (Fig. 2a, c). At $\Omega = 0$, these imaginary parts will take exactly the same ω_2-dependent profiles as shown in Fig. 1e, f, of course when ω_1 takes 0 and 1.4, respectively. Similarly, each MI map γ_{hj} is symmetric with respect to Ω and in the $\Omega \geq 0$ domain it is composed of one baseband part that has a limiting zero value at $\Omega = 0$ and some passbands that stand away from the central line $\Omega = 0$, as indicated in Fig. 2f, h. Generally, the appearance of passbands is a precursor of multiple rogue wave structures that could coexist on the same background[46]. It follows from Eqs. (4)–(6) that only the baseband of each MI spectrum determines the rogue wave domain[39,40], but either its baseband or passband may contribute to the rogue wave generation (Fig. 2l). In general, due to competition, the rogue wave structure associated with larger MI gain will be more prone to be excited, and hence occur more frequently, than the one with smaller MI gain.

The three families of Peregrine soliton states corresponding to the green crosses in Fig. 1f or 2k, which are denoted by I, II, and III, are demonstrated in Fig. 3, using $\omega_1 = 1.4$, $\omega_2 = \omega_1 + 2(\omega_1 - 1/\gamma)(\omega - 1/\omega + 1) \simeq 2.68$, $\omega_3 = (\omega_1 + \omega_2)/2 \simeq 2.04$, and the same a_j values as in Fig. 1. This set of initial parameters has been made to strictly fulfil the amplitude conditions (11) and hence the (μ, ν) values can be determined by Eqs. (12) (Case I), (13) (Case II), and (14) (Case III), respectively. It is exhibited that, in Case I (Fig. 3a), the u_1 component features the black rogue wave state whose amplitude falls to zero in

the dip center, while the u_2 and u_3 components manifest as the bright states, one of which (i.e., u_2) grows beyond the 3-fold amplitude. However, for Cases II and III, these field components may take other different structures, all localized in both space and time (Fig. 3b, c). Analytically, all these different rogue wave families are obtained with the same set of initial parameters, implying that they can coexist and develop on the same continuous background[63].

Numerical verification. We performed extensive numerical simulations to check our analytic predictions, using the exponential time differencing Crank–Nicolson (ETD-CN) and spectral method (see Methods for more detail)[79,80]. We first demonstrate in Fig. 4a–c the numerical solutions of the GNLS Eqs. (1) with $N = 3$, using the profiles of our analytic solutions (6) in the far region (namely, using $u_j(z = -3, t)$ for Case I rogue waves, and $u_j(z = -6, t)$ for the Case II and Case III rogue waves) as initial conditions, given the same set of system parameters as in Fig. 3. Note that, in Fig. 4a, a white noise of the strength that equals $0.1\%a_j$ has been put on the initial profiles, in order to excite MI waves earlier in a short distance. It is evident that these numerical solutions for all Case I, Case II, and Case III rogue waves exhibit excellent agreement with their analytic counterparts seen in Fig. 3 over a wide propagation range. Intriguingly, in our simulation results for Case III rogue waves (Fig. 4c), we also observe that there would occur Case I rogue waves on the same background (see arrows at around $z = 8$), which are not the outcome of input profiles, but result from the spontaneous MI. This confirms definitely the coexistence of two different types of rogue waves, for given set of system parameters. Now one may further wonder whether it is possible to see all three types of rogue waves on the same background, so as to conform to the MI-rogue wave correspondence established above.
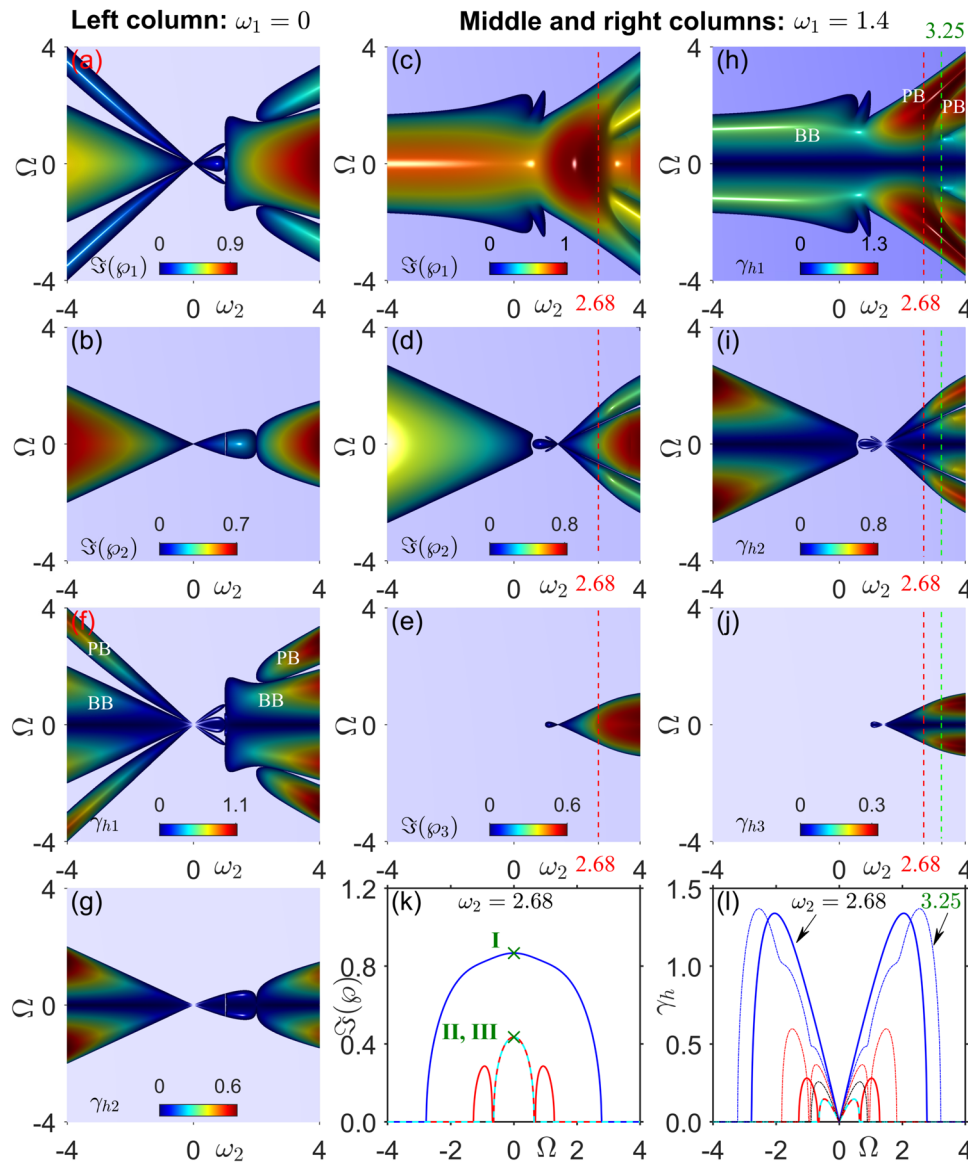
Fig. 2 Maps of $\Im(\wp_j)$ and $\gamma_{hj} = |\sigma\Omega\Im(\wp_j)|$ versus (ω_2, Ω). a–e Numerical results of the positive imaginary parts $\Im(\wp_j)$ calculated from Eq. (5) with respect to the central frequency ω_2 and the frequency offset Ω, for given (**a**, **b**) $\omega_1 = 0$ or (**c**, **d**, **e**) $\omega_1 = 1.4$. The other parameter conditions are same as in Fig. 1. **f–j** Maps of the corresponding modulation instability gains γ_{hj} with respect to (ω_2, Ω), for (**f**, **g**) $\omega_1 = 0$ or (**h**, **i**, **j**) $\omega_1 = 1.4$. The BB and PB in (**f**, **h**) are short for baseband and passband, respectively. In all maps, the colour bar on the bottom quantifies the magnitude of (**a–e**) $\Im(\wp_j)$ or (**f–j**) γ_{hj}. **k** Cross-sectional profiles of $\Im(\wp_j)$ along the red dashed lines in **c–e**, for given $\omega_1 = 1.4$ and $\omega_2 \simeq 2.68$. The green crosses in **k** indicate the values of ν for Cases I, II, and III that are identical to those in Fig. 1f. **l** Cross-sectional profiles of γ_{hj} along the red dashed lines at $\omega_2 \simeq 2.68$ in **h–j**. In **k**, **l**, blue solid curves stand for $\Im(\wp_1)$ and γ_{h1}, red solid curves for $\Im(\wp_2)$ and γ_{h2}, and cyan dashed curves for $\Im(\wp_3)$ and γ_{h3}. For the purpose of comparison, the cross-sectional gain profiles along the green dashed lines at $\omega_2 = 3.25$ in **h–j** are also illustrated in (**l**), denoted by thin dashed curves.

To confirm the latter issue, we then use in our numerical test the plane-wave solutions (2) at $z = 0$ perturbed by strong harmonic waves as initial conditions, which will soon develop into a turbulent sea of different waves (Fig. 4d). We find that, in this turbulent wave field, the three Peregrine solitons circled, respectively, by the ellipses I, II, and III at around $z = 2.52$, 6.85, and 2.93 can be identified as the corresponding ones shown in Fig. 3. This is more evident in the right and left insets therein, where a good agreement between the cross-sectional profiles (solid curves) at $z = 2.52$ and 2.93 and the corresponding analytic solutions (red dashed curves) can be seen. We should point out that the Peregrine rogue waves denoted by II have been strongly distorted by the surrounding waves, as compared to the patterns shown in Fig. 4b. Besides, one can observe that the Peregrine

soliton structures like Case I can appear in many places, but those like Cases II and III are much fewer (Fig. 4d). This is not surprising because Case I has a much larger MI gain value than the latter two, as seen by the bold curves in Fig. 2l, and naturally dominates the rogue wave occurrence. When the value of ω_2 is increased from 2.68 to 3.25, while keeping the background amplitudes a_j unchanged, one can observe more easily the coexistence of three types of rogue wave structures on the same background (Fig. 5), since now the related MI gain profiles become closer to each other, as seen by the thin dotted lines in Fig. 2l. Noting that in Fig. 5, we used the initial profiles denoted by
$$u_j(z=0, t) = u_{j0}[1 + iG_j^{(1)}(z-4, t)/M^{(1)}(z-4, t) + iG_j^{(2)}$$
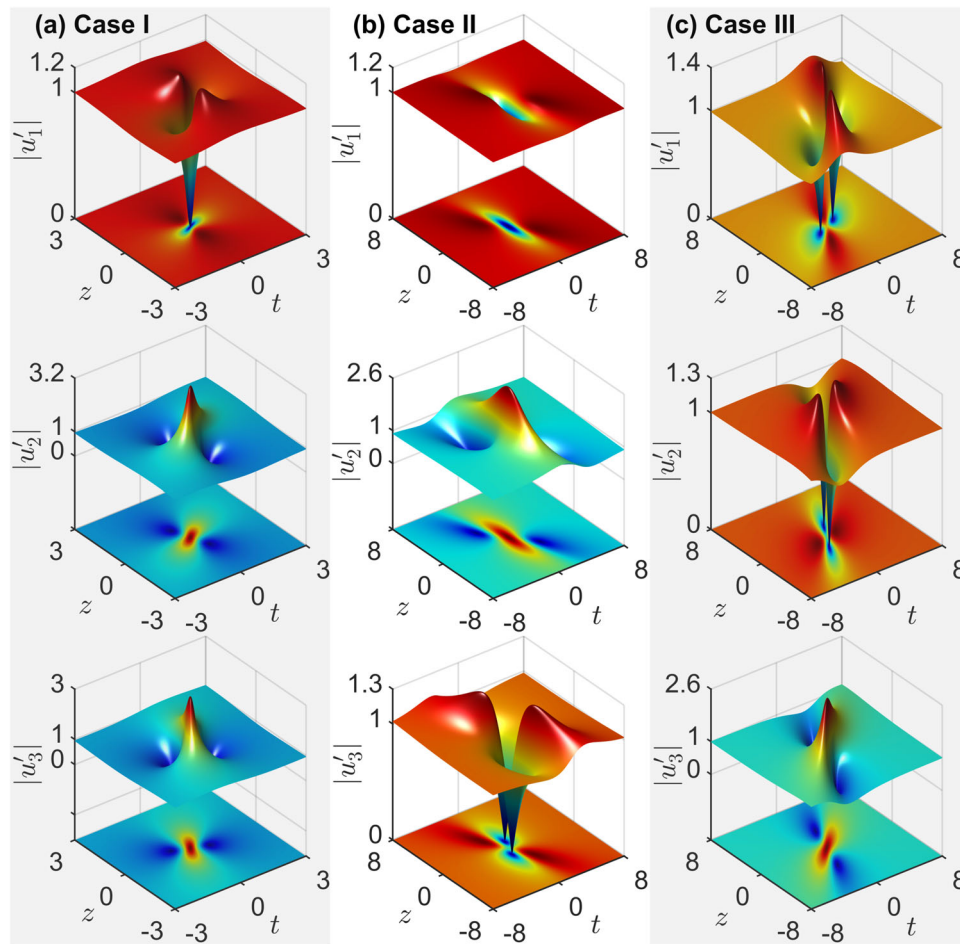$$(z-4, t+20)/M^{(2)}(z-4, t+20) + iG_j^{(3)}(z-4, t-20)/M^{(3)}$$

Fig. 3 Analytic results of three coexisting Peregrine soliton families on the continuous backgrounds. a–c 3D surface (top) and contour (bottom) plots of the analytic Peregrine soliton solutions (6) for three field components $u_{1,2,3}$. The real parameters μ and ν in the solutions are given by Eq. (12) for **a** Case I, by Eq. (13) for **b** Case II, and by Eq. (14) for **c** Case III, respectively. The same set of system parameters is used, which corresponds to the green crosses in Fig. 1f or 2k. Here all the rogue wave components have been normalized by their background heights a_j, denoted by $|u'_j| = |u_j/a_j|$.

$(z - 4, t - 20)]_{z=0}$, where M and G_j are defined by Eqs. (7) and (8), while the superscripts over them signify that the parameters μ and ν in these functions take (1) $\mu \simeq -2.3981$, $\nu \simeq 0.7674$, (2) $\mu \simeq -1.5515$, $\nu \simeq 0.5484$, and (3) $\mu \simeq -3.0254$, $\nu \simeq 0.6778$, respectively. This implies that the input profiles are a superposition of three well-separated yet low-amplitude rogue wave profiles, and thus can be thought of as some kind of strong perturbation to plane-wave solutions (2). Although the initial profiles are not the analytic solutions of the model equation, we observe that the rogue wave states numerically generated, as indicated by red arrows in Fig. 5a–c, could agree well with our analytic solutions (6). One can also notice that, for either set of parameters used in Fig. 4 or 5, there appear three different baseband MI spectra (Fig. 2h–j). Considering that three baseband MI spectra have resulted in three different rogue wave structures, our numerical results positively confirm the MI-rogue wave correspondence.

Corollary: Rogue waves on periodic backgrounds. Finally, we would like to point out that the GNLS model (1) owns an inherent SU(N) symmetry and hence any SU(N) group transformation of the solutions (6) will also give the new solutions u^p_j of the model, which can be expressed as

$$u^p_j = \sum_{m=1}^{N} \alpha_{jm} u_m, \quad j = 1, \cdots, N, \tag{15}$$

where u_m are the old rogue wave solutions (6), α_{jm} are the complex elements of the SU(N) matrix, $\mathbf{A} = (\alpha_{jm})_{N \times N}$, which should satisfy $\mathbf{A}\mathbf{A}^\dagger = \mathbf{A}^\dagger\mathbf{A} = 1$ and $\det(\mathbf{A}) = 1$. Demonstrably, the background fields, defined now by $u^b_j = \sum_{m=1}^N \alpha_{jm} u_{m0}$, could cause interference fringes that depend not only on the temporal beat frequencies $\delta_{mn} = \omega_m - \omega_n$, but also on the entries α_{jm} of $\mathbf{A}$, with the average background height

$$d_j = \left(\sum_{m=1}^{N} |\alpha_{jm}|^2 a_m^2 \right)^{1/2}. \tag{16}$$

In this regard, the solutions defined by Eq. (15) will represent the rogue wave states developed on the periodic backgrounds, as demonstrated in ref. [46] where $N = 2$.

For illustration, we still consider $N = 3$ case (see Supplementary Note 4 for detailed information) and demonstrate in Fig. 6 three families of rogue wave states sitting on the periodic backgrounds, using the same set of initial parameters as in Fig. 3, but with

$$\mathbf{A} = \begin{bmatrix} \sqrt{3}/4 - \sqrt{6}/8 & 1/4 + 3\sqrt{2}/8 & \sqrt{6}/4 \\ -3/4 - \sqrt{2}/8 & -\sqrt{3}/4 + \sqrt{6}/8 & \sqrt{2}/4 \\ \sqrt{2}/4 & -\sqrt{6}/4 & \sqrt{2}/2 \end{bmatrix}. \tag{17}$$

It is seen that all backgrounds that support the rogue waves become now periodic, owing to the constructive or destructive interferences between three continuous waves. Despite their
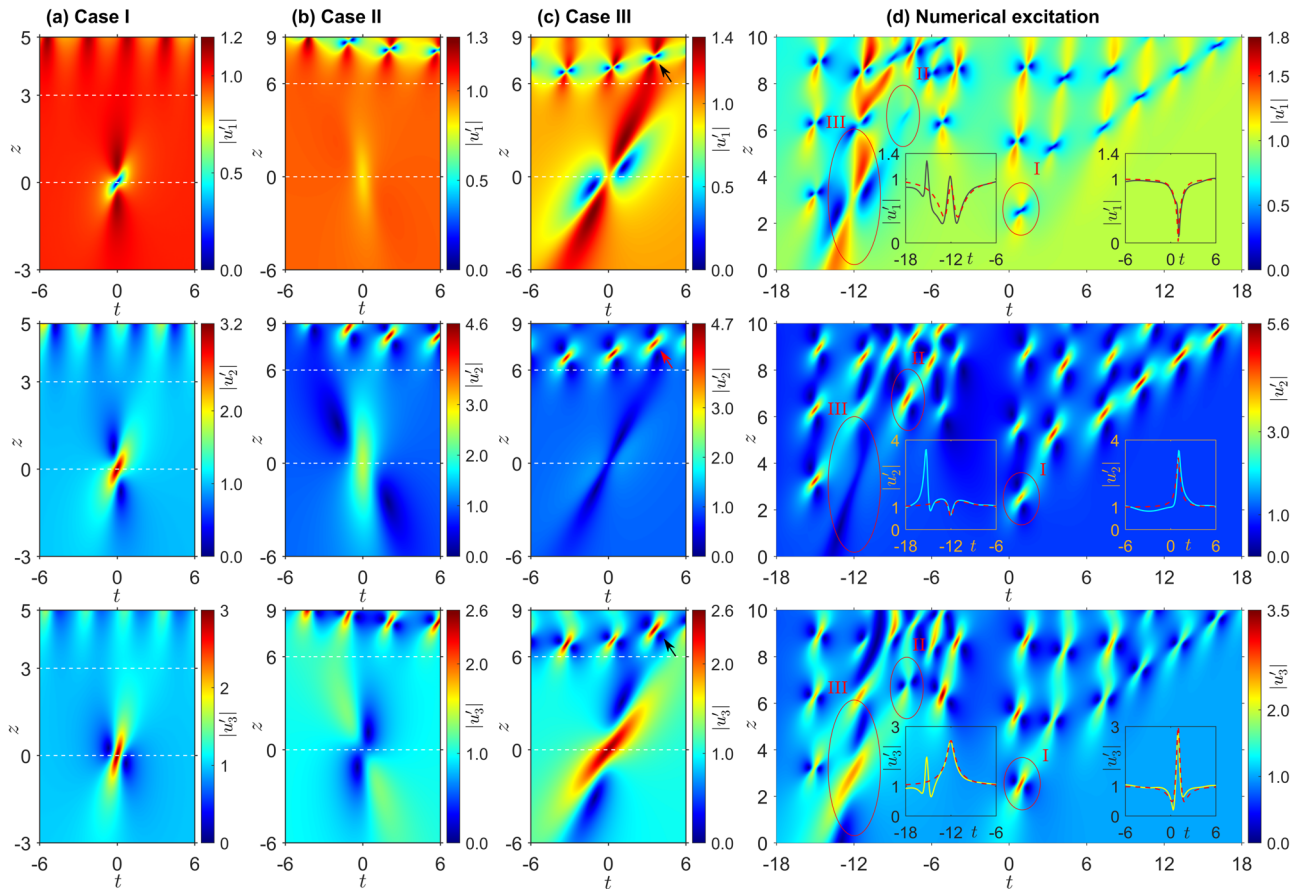
Fig. 4 Numerical simulations of three coexisting Peregrine solitons and their numerical excitation. a–c Numerical simulation results of Case I, Case II, and Case III rogue wave states seen in Fig. 3. To produce them, we integrate Eqs. (1) ($N = 3$) using the exponential time differencing Crank--Nicolson scheme armed with (3, 3)-order Padé approximation. The initial profiles for numerics are taken to be the analytical solutions at **a** $z = -3$ and **b, c** $z = -6$, respectively. It is exhibited that all rogue wave states can be numerically reproduced till the far trailing region where the periodic wave trains begin to appear. The arrows in (**c**) indicate a wave state that takes after Case I rogue wave. **d** Numerical excitation of three coexisting Peregrine solitons from a turbulent field. The initial condition is now supposed to be the plane-wave solutions (2) at $z = 0$ perturbed by strong harmonic waves, with other system parameters the same as in Fig. 3. The ellipses I, II, and III have singled out these Peregrine soliton structures. The right and left insets show the comparison of the cross-sectional profiles (solid curves) at $z = 2.52$ and 2.93 with the analytic solutions (red dashed curves) for Case I and Case III rogue waves, respectively. In all panels, the colour bar on the right quantifies the magnitude of the normalized amplitude $|u'_j| = |u_j/a_j|$, where a_j is the background height.

multifarious patterns, however, the occurrence of such periodic rogue waves are still governed by the MI evolution Eq. (5), namely, by the MI-rogue wave correspondence.

Conclusion

In conclusion, we established an explicit universal one-to-one correspondence between the baseband MI and the Peregrine rogue wave solutions, with which complex rogue wave dynamics as well as their signatures can be unveiled. Such MI-rogue wave correspondence is an analog of the bulk-boundary correspondence in topological physics, with rogue waves corresponding to the edge modes and MI corresponding to the bulk topological invariant, respectively. We exemplified this MI-rogue wave correspondence with the specific three-component GNLS model and numerically confirmed the excitation of three coexisting Peregrine solitons from a turbulent wave field, which exactly occurs as predicted by the MI analysis. In view of that MI is a particular feature of nonlinear systems, whether they are integrable or not, we expect the MI-rogue wave correspondence to be applicable to non-integrable systems as well, just as the bulk-boundary correspondence can work in non-Hermitian systems[34–36]. In that sense, our work unequivocally substantiates the insight that MI is the most fundamental mechanism underlying the rogue wave formation.

Given the MI-rogue wave correspondence established above, our work also offers an alternative way of obtaining exact rogue wave solutions from the MI analysis. In the Methods section, we provide an example to expatiate how to figure out the exact general fundamental rogue wave solutions of the three-wave resonant interaction (TWRI) equation[81–83] from the MI analysis instead of from the complicated Darboux transformation or Hirota bilinearization[84]. It should be mentioned that the closed-form solutions thus obtained are much clearer in form than those reported most recently in ref. [84].

Methods

The MI equation for GNLS model. Here we outline the derivation of the MI evolution Eq. (5) within the multi-component GNLS equation framework. More derivation details along with the obtainment of rogue wave solutions can be found in Supplementary Note 1.

It is easy to check that this GNLS model admits the plane-wave solutions (2). Because of MI induced by nonlinearity and noises, such cw backgrounds are highly unstable and will eventually develop into a sea of waves, from which a series of high-contrast peaks of random intensity can be identified. Basically, the MI gain can be obtained via the linear stability analysis, which assumes the above plane-wave solutions to be perturbed according to Eqs. (4), where the terms associated with r_j and w_j represents the small-amplitude Fourier modes. Subsequently, substitution of Eqs. (4) into Eqs. (1) followed by a collection of the linear terms
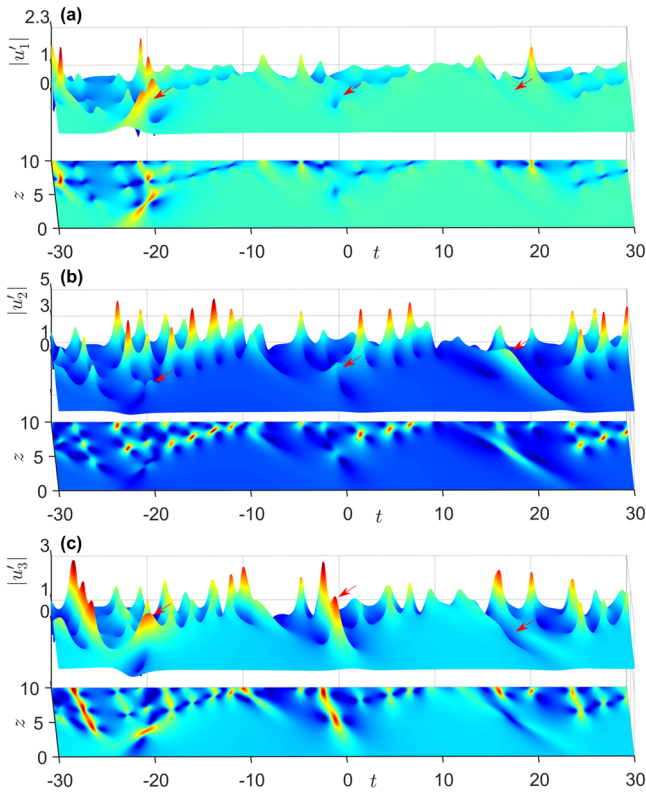
Fig. 5 Numerical excitation of three Peregrine soliton families. Numerical simulation results for the **a** u_1, **b** u_2, and **c** u_3 field components, which develop on the backgrounds that allow the modulation instability spectra indicated by thin dashed lines in Fig. 2l. Different from Fig. 4d, we now use the initial condition defined by a superposition of three well-separated low-amplitude rogue wave profiles. The input frequencies are given by $\omega_1 = 1.4$, $\omega_2 = 3.25$, and $\omega_3 = (\omega_1 + \omega_2)/2 = 2.325$, while the other parameters are kept the same as in Fig. 2. This set of system parameters would yield: (1) $\mu \simeq -2.3981$, $\nu \simeq 0.7674$; (2) $\mu \simeq -1.5515$, $\nu \simeq 0.5484$; and (3) $\mu \simeq -3.0254$, $\nu \simeq 0.6778$. All field components are normalized by their respective backgrounds and the red arrows mark out three Peregrine soliton structures that exhibit a good agreement with the analytic solutions (6).

yields a system of $2N$ coupled linear equations about r_j and w_j:

$$\sigma\Omega\left(\frac{\Omega}{2} + \wp + \omega_j\right)r_j + v_j\sum_{m=1}^{N}a_m^2 r_m + v_j\sum_{m=1}^{N}a_m^2 w_m = 0, \quad (18)$$

$$\sigma\Omega\left(\frac{\Omega}{2} - \wp - \omega_j\right)w_j + v_j\sum_{m=1}^{N}a_m^2 r_m + v_j\sum_{m=1}^{N}a_m^2 w_m = 0, \quad (19)$$

where $j = 1,...,N$ and $\wp = (A\gamma + \varkappa)/\sigma$. This system of equations has a nontrivial solution only when the determinant of the coefficient matrix of the vector $(r_1, \cdots, r_N, w_1, \cdots, w_N)^T$ equals zero. By elementary transformations of the coefficient matrix, one can easily obtain Eq. (5), which defines the evolution of MI for any complex $\wp$ or $\varkappa$.

Simulations. In our simulations for Figs. 4 and 5, an efficient, second-order convergent, ETD-CN method was used[79,80]. Specifically, Eqs. (1) can be rewritten, in the spectral domain, as

$$\frac{\partial \tilde{u}_j}{\partial z} + L\tilde{u}_j = \tilde{F}(z, u_j), \quad (20)$$

where $\tilde{u}_j$ is the fast Fourier transform, which we will denote by the symbol $\mathcal{F}$ below, of the wave component u_j with respect to time, namely, $\tilde{u}_j = \mathcal{F}(u_j)$, $L = i\sigma\omega^2/2$ is the linear operator with ω being the transformed frequency variable, and $\tilde{F}(z, u_j)$ is the fast Fourier transform of the nonlinear term, i.e., $\tilde{F}(z, u_j) = \mathcal{F}\left[i(\sum_{m=1}^{N}|u_m|^2)(u_j + i\gamma\frac{\partial u_j}{\partial t})\right]$. Then, let $h = z_{n+1} - z_n$ be the spatial step size, we arrive at the following recurrence formulas based on the ETD-

CN scheme[79]:

$$\tilde{b}_{jn} = \mathcal{R}_1\tilde{u}_{jn} + \mathcal{R}_2\tilde{F}(z_n, u_{jn}), \quad (21)$$

$$\tilde{u}_{j(n+1)} = \tilde{b}_{jn} + \mathcal{R}_3[\tilde{F}(z_n + h, \mathcal{F}^{-1}(\tilde{b}_{jn})) - \tilde{F}(z_n, u_{jn})], \quad (22)$$

where

$$\mathcal{R}_1 = e^{-hL}, \quad \mathcal{R}_2 = -\frac{e^{-hL} - I}{L}, \quad \mathcal{R}_3 = \frac{e^{-hL} - I + hL}{hL^2}, \quad (23)$$

with I being the identity operator. To achieve higher spectral (or equivalently, temporal) accuracy, we now use $(3,3)$-order Padé approximation for the exponential matrix e^{-hL}, i.e.,

$$e^{-hL} \simeq \frac{120I - 60hL + 12h^2L^2 - h^3L^3}{120I + 60hL + 12h^2L^2 + h^3L^3} \equiv \mathcal{R}_1. \quad (24)$$

Then $\mathcal{R}_2$ and $\mathcal{R}_3$ can also be transformed into the rational polynomials via Eq. (24). Basically, by using Eqs. (21)–(24), the coupled spectral Eqs. (20) can be numerically solved with high accuracy. Finally, an inverse fast Fourier transform of $\tilde{u}_j$ yields the numerical solutions u_j of GNLS Eqs. (1).

Specifically, in our simulations, we used the simulation window of t in the range $[-800, 800]$, with the time step size $\Delta t = 0.006$. The spatial step size h should be chosen smaller (here, $h = 5 \times 10^{-4}$) so that $h\pi/\Delta t < 1$, which will ensure the $(3,3)$-order Padé approximation (24) for e^{-hL} to be accurate enough over the whole spectral domain. Despite the large simulation window, we only present what happens in the central portion, say, in $[-18, 18]$ in Fig. 4d. Basically, any numerical algorithms can bring numerical errors, which will serve as intrinsic numerical noise to excite spontaneous MI. In our numerics, we also imposed strong external perturbations (e.g., white noise or harmonic waves) in order to excite MI as early as possible, so that we can observe the occurrence of rogue waves within shorter propagation distance.

MI–rogue wave correspondence in other integrable systems. We now demonstrate the MI-rogue wave correspondence in other different integrable systems, i.e., the vector Kaup–Newell equation[19] and the $(2+1)$-component long-wave short-wave resonance equation[63]. Although the fundamental rogue wave solutions have been reported for these models, their intimate relation to MI was not revealed therein.

(i) Kaup–Newell model. We first consider the vector Kaup–Newell model which can be written as[19]

$$i\frac{\partial u_j}{\partial z} + \frac{\sigma}{2}\frac{\partial^2 u_j}{\partial t^2} + \left(1 + i\gamma\frac{\partial}{\partial t}\right)[(|u_1|^2 + |u_2|^2)u_j] = 0, \quad (25)$$

where $j = 1, 2$, and the parameter γ accounts for the self-steepening effect often seen by pulses with spectral widths comparable to the optical frequency. This two-component model possesses the plane-wave solutions:

$$u_{j0} = a_j\exp(i\omega_j t - ik_j z), \quad j = 1, 2, \quad (26)$$

where

$$k_j = A(\gamma\omega_j - 1) + \frac{1}{2}\sigma\omega_j^2, \quad A = \sum_{j=1}^{2}a_j^2 = a_1^2 + a_2^2. \quad$$

We assume that these plane-wave solutions are perturbed by the same Fourier modes as in Eqs. (4). A direct MI analysis of them results in a system of four linear equations for $r_{1,2}$ and $w_{1,2}$. It is easy to show that this system of linear equations has a nontrivial solution only when the dispersion relation (see Supplementary Note 3 for detailed derivation)

$$\frac{a_1^2(2\gamma\wp + \gamma\omega_1 + 1)}{(\wp + \omega_1)^2 - \Omega^2/4} + \frac{a_2^2(2\gamma\wp + \gamma\omega_2 + 1)}{(\wp + \omega_2)^2 - \Omega^2/4} + \sigma = 0, \quad (27)$$

is satisfied. It is seen that the dispersion relation Eq. (27) has a more complicated form than Eq. (5). This implies that the rogue wave solutions of the vector Eqs. (25) will be quite different from those of the vector GNLS Eqs. (1).

In fact, it has been reported in ref. [19] that the general fundamental rogue wave solutions can take the form

$$u_j = u_{j0}\left(1 + \frac{R_j}{M - iK}\right)\left(\frac{M + iK}{M - iK}\right), \quad (28)$$

where the polynomials M, K, $R_{1,2}$ are defined by

$$M = \tau^2 + \sigma^2\nu^2 z^2 + \frac{\eta^2}{4\alpha\nu^2}, \quad K = \frac{\gamma}{\alpha}(\sigma\gamma\nu^2 z - \eta\tau), \quad (29)$$

$$R_j = \frac{2i[(\mu + \omega_j)\tau - \sigma\nu^2 z]}{(\mu + \omega_j)^2 + \nu^2} - \frac{2\alpha + \eta(\gamma\omega_j - 1)}{\alpha[(\mu + \omega_j)^2 + \nu^2]}, \quad (30)$$

with $\tau = t + (\sigma\mu - \gamma A)z$, $\eta = \gamma\mu + 1$, and $\alpha = \nu^2\gamma^2 + \eta^2$. The real parameters μ and ν in Eqs. (29) and (30) are determined by the complex root $\wp = \mu + i\nu$ of the quartic equation:

$$\frac{a_1^2(2\gamma\wp + \gamma\omega_1 + 1)}{(\wp + \omega_1)^2} + \frac{a_2^2(2\gamma\wp + \gamma\omega_2 + 1)}{(\wp + \omega_2)^2} + \sigma = 0. \quad (31)$$
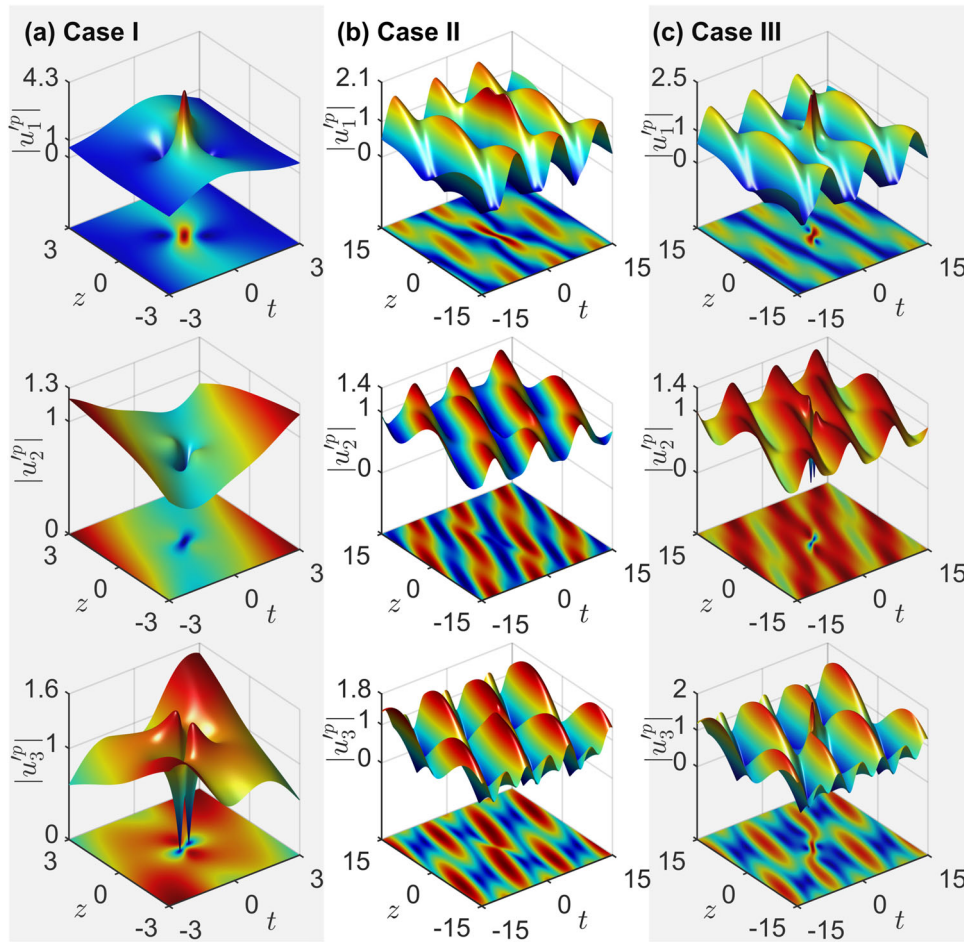
Fig. 6 Peregrine solitons on the periodic backgrounds. a–c 3D surface (top) and contour (bottom) plots of the Peregrine soliton solutions (15) on the periodic backgrounds characterized by the coefficient matrix (17), with system parameters all the same as in Fig. 3. This set of parameters could result in : **a** $\mu \simeq -2.0384$, $\nu \simeq 0.8682$; **b** $\mu \simeq -2.4355$, $\nu \simeq 0.4341$; and (**c**) $\mu \simeq -1.6413$, $\nu \simeq 0.4341$, exactly the same as indicated by green crosses in Fig. 1f or 2k. Here all the rogue wave components are normalized as $|u_j'^p| = |u_j^p|/d_j$, where d_j is the average background height defined by Eq. (16).

Once again, the characteristic Eq. (31) is the same as the dispersion relation Eq. (27) in the baseband limit $\Omega = 0$, although they are derived in a different way.

(ii) Long-wave short-wave model. We then demonstrate the MI-rogue wave correspondence in the (2+1)-component long-wave short-wave model, which describes the nonlinear interaction between two complex short-wave field envelopes, $u_{1,2}$, and the real long-wave field, ϕ. In dimensionless form, this multi-component model reads[63]

$$\mathrm{i}\frac{\partial u_j}{\partial z} + \frac{1}{2}\frac{\partial^2 u_j}{\partial t^2} + u_j\phi = 0, \quad (j = 1, 2),$$
$$\frac{\partial \phi}{\partial z} - \frac{\partial}{\partial t}(|u_1|^2 + |u_2|^2) = 0, \tag{32}$$

where t and z are two independent variables. The plane-wave solutions of this model can be easily found to be

$$u_{j0} = a_j \exp(\mathrm{i}\omega_j t - \mathrm{i}k_j z), \tag{33}$$

where $k_j = \frac{1}{2}\omega_j^2 - b$ and $b \geqslant 0$ defines the background of the real long-wave field.

In a similar fashion, substituting the following perturbed plane-wave solutions

$$u_j = u_{j0}\{1 + r_j \exp[\mathrm{i}\Omega(\kappa z + t)] + w_j^* \exp[-\mathrm{i}\Omega(\kappa^* z + t)]\}, \tag{34}$$

$$\phi = b + p \exp[\mathrm{i}\Omega(\kappa z + t)] + p^* \exp[-\mathrm{i}\Omega(\kappa^* z + t)], \tag{35}$$

into Eqs. (32) and collecting the linear terms, one can obtain a system of five coupled equations. As noted in linear algebra, only when its coefficient matrix has a zero determinant does the vector $(r_1, r_2, w_1, w_2, p)^T$ have a nontrivial solution. This zero determinant condition can give rise to the following dispersion relation (see Supplementary Note 3):

$$\frac{a_1^2}{(\kappa + \omega_1)^2 - \Omega^2/4} + \frac{a_2^2}{(\kappa + \omega_2)^2 - \Omega^2/4} + \kappa = 0, \tag{36}$$

which is now a quintic equation of κ.

On the other hand, the general fundamental rogue wave solutions of Eqs. (32) can be written as[63]

$$u_j = u_{j0}\left\{1 - \frac{2\mathrm{i}\nu^2 z - 2\mathrm{i}(\mu + \omega_j)(t + \mu z) + 1}{[(\mu + \omega_j)^2 + \nu^2][(t + \mu z)^2 + \nu^2 z^2 + 1/(4\nu^2)]}\right\}, \tag{37}$$

$$\phi = b + \frac{2[\nu^2 z^2 - (t + \mu z)^2 + 1/(4\nu^2)]}{[(t + \mu z)^2 + \nu^2 z^2 + 1/(4\nu^2)]^2}. \tag{38}$$

As demonstrated in the preceding example, the real parameters μ and ν in Eqs. (37) and (38) are again determined by the dispersion relation Eq. (36) in the baseband limit $\Omega = 0$, that is, by the following quintic equation of $\kappa = \mu + \mathrm{i}\nu$:

$$\frac{a_1^2}{(\kappa + \omega_1)^2} + \frac{a_2^2}{(\kappa + \omega_2)^2} + \kappa = 0. \tag{39}$$

Another route to exact rogue wave solutions. Finally, let us demonstrate how to figure out the exact rogue wave solutions from the MI analysis, based on the MI-rogue wave correspondence established (see Supplementary Note 5 for more detail). We limit our attention to the popular TWRI equation, which enjoys a prominent status in nonlinear optics[81]. In dimensionless form, the TWRI model reads[81–83]

$$\frac{\partial u_1}{\partial t} + V_1 \frac{\partial u_1}{\partial z} = u_2^* u_3^*, \quad \frac{\partial u_2}{\partial t} + V_2 \frac{\partial u_2}{\partial z} = -u_1^* u_3^*,$$
$$\frac{\partial u_3}{\partial t} + V_3 \frac{\partial u_3}{\partial z} = u_1^* u_2^*, \tag{40}$$

where $u_{1,2,3}(z, t)$ are the slowly varying complex envelopes of three wave fields. The coefficients V_j correspond to the relative group velocities of three waves and we suppose $V_{1,2} > V_3$. Without loss of generality, we set $V_3 = 0$, which implies that Eqs. (40) are written in a reference frame comoving with u_3.

9

Hence, the initial plane-wave solutions that satisfy Eqs. (40) can be found to be

$$
\begin{aligned}
u_{10}(z,t) &= a_1 \exp\left[-i(k_1 z - \omega_1 t)\right], \\
u_{20}(z,t) &= a_2 \exp\left[i(k_2 z - \omega_2 t)\right], \\
u_{30}(z,t) &= i a_3 \exp\left[i(k_1 - k_2)z - i(\omega_1 - \omega_2)t\right],
\end{aligned}
\tag{41}
$$

where

$$
k_1 = \frac{\omega_1}{V_1} + \frac{a_2^2}{\delta V_1}, \quad k_2 = \frac{\omega_2}{V_2} + \frac{a_1^2}{\delta V_2}, \quad a_3 = \frac{a_1 a_2}{\delta},
\tag{42}
$$

with $a_{1,2,3}$ being the background heights and $\delta = \omega_1 - \omega_2$. Subsequently, substituting the perturbed plane-wave solutions

$$
u_j = u_{j0}\{1 + r_j \exp[i\Omega(\kappa z + t)] + w_j^* \exp[-i\Omega(\kappa^* z + t)]\},
\tag{43}
$$

where $j = 1, 2, 3$, into the TWRI equation followed by linearization, one can obtain a system of six coupled equations. Under the condition that the system of equations admits only nontrivial solutions, one can find the dispersion relation:

$$
\left(\frac{a_1^2}{V_2\kappa + 1} + \frac{a_2^2}{V_1\kappa + 1}\right)^2 + 2\delta^2\left(\frac{a_1^2}{V_2\kappa + 1} - \frac{a_2^2}{V_1\kappa + 1}\right) + \delta^4 = \Omega^2\delta^2.
\tag{44}
$$

Now, to find the rogue wave solutions, we first assume $\Omega = 0$ in Eq. (44) and rewrite it as

$$
\left(\frac{a_1^2}{V_2\kappa + 1} + \frac{a_2^2}{V_1\kappa + 1}\right)^2 + 2\delta^2\left(\frac{a_1^2}{V_2\kappa + 1} - \frac{a_2^2}{V_1\kappa + 1}\right) + \delta^4 = 0,
\tag{45}
$$

which can give the values of $\kappa = \mu + i\nu$ for given set of system parameters. Then we suppose the rogue wave solutions to take

$$
\begin{aligned}
u_1 &= u_{10}\left[1 + \frac{if_1(t + \mu z) + ig_1 z + e_1}{(t + \mu z)^2 + \nu^2 z^2 + 1/\alpha}\right], \\
u_2 &= u_{20}\left[1 + \frac{if_2(t + \mu z) + ig_2 z + e_2}{(t + \mu z)^2 + \nu^2 z^2 + 1/\alpha}\right], \\
u_3 &= u_{30}\left[1 - \frac{if_3(t + \mu z) + ig_3 z + e_3}{(t + \mu z)^2 + \nu^2 z^2 + 1/\alpha}\right],
\end{aligned}
\tag{46}
$$

where the real parameters $e_{1,2,3}$, $f_{1,2,3}$, $g_{1,2,3}$, and α are to be determined. Substituting Eqs. (46) into the TWRI Eqs. (40) and equating the coefficients of $z^l t^m$ (l, m are powers) to zero, one can readily find that

$$
f_1 = \frac{\sqrt{2(\ell_2 - V_2\mu - 1)}}{a_1}, \quad g_1 = -\frac{\nu\sqrt{2(\ell_2 + V_2\mu + 1)}}{a_1},
\tag{47}
$$

$$
f_2 = \frac{\sqrt{2(\ell_1 + V_1\mu + 1)}}{a_2}, \quad g_2 = \frac{\nu\sqrt{2(\ell_1 - V_1\mu - 1)}}{a_2},
\tag{48}
$$

$$
\ell_j = \sqrt{(V_j\mu + 1)^2 + V_j^2\nu^2}, \quad (j = 1, 2),
\tag{49}
$$

$$
\alpha = \frac{16\nu^2 g_1^2}{(f_1^2\nu^2 + g_1^2)^2} = \frac{16\nu^2 g_2^2}{(f_2^2\nu^2 + g_2^2)^2},
\tag{50}
$$

$$
e_1 = -\frac{f_1^2}{4} - \frac{g_1^2}{4\nu^2}, \quad e_2 = -\frac{f_2^2}{4} - \frac{g_2^2}{4\nu^2},
\tag{51}
$$

$$
f_3 = f_1 + f_2, \quad g_3 = g_1 + g_2, \quad e_3 = f_1 f_2 - (e_1 + e_2) - \frac{f_1 + f_2}{\delta}.
\tag{52}
$$

It is seen that all these coefficients have been uniquely determined by the real parameters μ and ν, and hence, according to Eqs. (46), the resultant fundamental rogue wave solutions of the TWRI equation are obtained.

Data availability

Raw numerical data for the plots and all analytic derivations based on the Maple software are available from the corresponding authors upon request.

Code availability

All numerical codes are generated based on the commercial software Matlab and are only available from the corresponding authors upon reasonable request.

References

1. Dysthe, K., Krogstad, H. E. & Müller, P. Oceanic rogue waves. *Annu. Rev. Fluid Mech.* **40**, 287–310 (2008).
2. Chabchoub, A., Hoffmann, N. P. & Akhmediev, N. Rogue wave observation in a water wave tank. *Phys. Rev. Lett.* **106**, 204502 (2011).
3. Dematteis, G., Grafke, T., Onorato, M. & Vanden-Eijnden, E. Experimental evidence of hydrodynamic instantons: the universal route to rogue waves. *Phys. Rev. X* **9**, 041057 (2019).
4. Solli, D. R., Ropers, C., Koonath, P. & Jalali, B. Optical rogue waves. *Nature* **450**, 1054–1057 (2007).
5. Lecaplain, C., Grelu, P., Soto-Crespo, J. M. & Akhmediev, N. Dissipative rogue waves generated by chaotic pulse bunching in a mode-locked laser. *Phys. Rev. Lett.* **108**, 233901 (2012).
6. Dudley, J. M., Genty, G., Mussot, A., Chabchoub, A. & Dias, F. Rogue waves and analogies in optics and oceanography. *Nat. Rev. Phys.* **1**, 675–689 (2019).
7. Tsai, Y.-Y., Tsai, J.-Y. & I, L. Generation of acoustic rogue waves in dusty plasmas through three-dimensional particle focusing by distorted waveforms. *Nat. Phys.* **12**, 573–577 (2016).
8. Bludov, Y. V., Konotop, V. V. & Akhmediev, N. Matter rogue waves. *Phys. Rev. A* **80**, 033610 (2009).
9. Närhi, M. et al. Machine learning analysis of extreme events in optical fibre modulation instability. *Nat. Commun.* **9**, 4923 (2018).
10. Marcucci, G., Pierangeli, D. & Conti, C. Theory of neuromorphic computing by waves: machine learning by rogue waves, dispersive shocks, and solitons. *Phys. Rev. Lett.* **125**, 093901 (2020).
11. Baronio, F., Degasperis, A., Conforti, M. & Wabnitz, S. Solutions of the vector nonlinear Schrödinger equations: evidence for deterministic rogue waves. *Phys. Rev. Lett.* **109**, 044102 (2012).
12. Chen, S., Baronio, F., Soto-Crespo, J. M., Grelu, P. & Mihalache, D. Versatile rogue waves in scalar, vector, and multidimensional nonlinear systems. *J. Phys. A: Math. Theor.* **50**, 463001 (2017).
13. Peregrine, D. H. Water waves, nonlinear Schrödinger equations and their solutions. *J. Aust. Math. Soc. Ser. B, Appl. Math.* **25**, 16–43 (1983).
14. Shrira, V. I. & Geogjaev, V. V. What makes the Peregrine soliton so special as a prototype of freak waves? *J. Eng. Math.* **67**, 11–22 (2010).
15. Tikan, A. et al. Universality of the Peregrine soliton in the focusing dynamics of the cubic nonlinear Schrödinger equation. *Phys. Rev. Lett.* **119**, 033901 (2017).
16. Onorato, M., Residori, S., Bortolozzo, U., Montina, A. & Arecchi, F. T. Rogue waves and their generating mechanisms in different physical contexts. *Phys. Rep.* **528**, 47–89 (2013).
17. Dudley, J. M., Dias, F., Erkintalo, M. & Genty, G. Instabilities, breathers and rogue waves in optics. *Nat. Photon.* **8**, 755–764 (2014).
18. Chen, S., Ye, Y., Soto-Crespo, J. M., Grelu, P. & Baronio, F. Peregrine solitons beyond the threefold limit and their two-soliton interactions. *Phys. Rev. Lett.* **121**, 104101 (2018).
19. Chen, S., Pan, C., Grelu, P., Baronio, F. & Akhmediev, N. Fundamental Peregrine solitons of ultrastrong amplitude enhancement through self-steepening in vector nonlinear systems. *Phys. Rev. Lett.* **124**, 113901 (2020).
20. Kibler, B. et al. The Peregrine soliton in nonlinear fibre optics. *Nat. Phys.* **6**, 790–795 (2010).
21. Bailung, H., Sharma, S. K. & Nakamura, Y. Observation of Peregrine solitons in a multicomponent plasma with negative ions. *Phys. Rev. Lett.* **107**, 255005 (2011).
22. Chabchoub, A. Tracking breather dynamics in irregular sea state conditions. *Phys. Rev. Lett.* **117**, 144103 (2016).
23. Kane, C. & Lubensky, T. Topological boundary modes in isostatic lattices. *Nat. Phys.* **10**, 39–45 (2014).
24. Lu, L., Joannopoulos, J. & Soljačić, M. Topological photonics. *Nat. Photon.* **8**, 821–829 (2014).
25. Randoux, S., Suret, P. & El, G. Inverse scattering transform analysis of rogue waves using local periodization procedure. *Sci. Rep.* **6**, 29238 (2016).
26. Li, L., Mu, S., Lee, C. H. & Gong, J. Quantized classical response from spectral winding topology. *Nat. Commun.* **12**, 5294 (2021).
27. Guo, C. X., Liu, C. H., Zhao, X.-M., Liu, Y. & Chen, S. Exact solution of non-Hermitian systems with generalized boundary conditions: size-dependent boundary effect and fragility of the skin effect. *Phys. Rev. Lett.* **127**, 116801 (2021).
28. Wang, Z., Chong, Y., Joannopoulos, J. D. & Soljačić, M. Observation of unidirectional backscattering-immune topological electromagnetic states. *Nature* **461**, 772–775 (2009).
29. Baronio, F., Chen, S. & Mihalache, D. Two-color walking Peregrine solitary waves. *Opt. Lett.* **42**, 3514–3517 (2017).
30. Coulais, C., Fleury, R. & van Wezel, J. Topology and broken Hermiticity. *Nat. Phys.* **17**, 9–13 (2021).
31. Marcucci, G. et al. Topological control of extreme waves. *Nat. Commun.* **10**, 5090 (2019).

32. Thouless, D. J., Kohmoto, M., Nightingale, M. P. & Nijs, M. D. Quantized Hall conductance in a two-dimensional periodic potential. *Phys. Rev. Lett.* **49**, 405–408 (1982).

33. Silveirinha, M. G. Proof of the bulk-edge correspondence through a link between topological photonics and fluctuation-electrodynamics. *Phys. Rev. X* **9**, 011037 (2019).

34. Fu, Y. & Qin, H. Topological phases and bulk-edge correspondence of magnetized cold plasmas. *Nat. Commun.* **12**, 3924 (2021).

35. Helbig, T. et al. Generalized bulk-boundary correspondence in non-Hermitian topolectrical circuits. *Nat. Phys.* **16**, 747–750 (2020).

36. Xiao, L. et al. Non-Hermitian bulk-boundary correspondence in quantum dynamics. *Nat. Phys.* **16**, 761–766 (2020).

37. Akhmediev, N. N. & Korneev, V. I. Modulation instability and periodic solutions of the nonlinear Schrödinger equation. *Theor. Math. Phys.* **69**, 1089–1093 (1986).

38. Onorato, M., Osborne, A. R. & Serio, M. Modulational instability in crossing sea states: a possible mechanism for the formation of freak waves. *Phys. Rev. Lett.* **96**, 014503 (2006).

39. Baronio, F. et al. Vector rogue waves and baseband modulation instability in the defocusing regime. *Phys. Rev. Lett.* **113**, 034101 (2014).

40. Baronio, F., Chen, S., Grelu, P., Wabnitz, S. & Conforti, M. Baseband modulation instability as the origin of rogue waves. *Phys. Rev. A* **91**, 033804 (2015).

41. Kibler, B., Chabchoub, A., Gelash, A., Akhmediev, N. & Zakharov, V. E. Superregular breathers in optics and hydrodynamics: omnipresent modulation instability beyond simple periodicity. *Phys. Rev. X* **5**, 041026 (2015).

42. Toenger, S. et al. Emergent rogue wave structures and statistics in spontaneous modulation instability. *Sci. Rep.* **5**, 10380 (2015).

43. Pierangeli, D. et al. Observation of Fermi-Pasta-Ulam-Tsingou recurrence and its exact dynamics. *Phys. Rev. X* **8**, 041017 (2018).

44. Xu, G., Chabchoub, A., Pelinovsky, D. E. & Kibler, B. Observation of modulation instability and rogue breathers on stationary periodic waves. *Phys. Rev. Res.* **2**, 033528 (2020).

45. Vanderhaegen, G. et al. "Extraordinary" modulation instability in optics and hydrodynamics. *Proc. Natl Acad. Sci. USA* **118**, e2019348118 (2021).

46. Pan, C. et al. Omnipresent coexistence of rogue waves in a nonlinear two-wave interference system and its explanation by modulation instability. *Phys. Rev. Res.* **3**, 033152 (2021).

47. Benjamin, T. B. & Feir, J. E. The disintegration of wave trains on deep water. Part 1: theory. *J. Fluid Mech.* **27**, 417–430 (1967).

48. Walczak, P., Randoux, S. & Suret, P. Optical rogue waves in integrable turbulence. *Phys. Rev. Lett.* **114**, 143903 (2015).

49. Suret, P. et al. Single-shot observation of optical rogue waves in integrable turbulence using time microscopy. *Nat. Commun.* **7**, 13136 (2016).

50. Frisquet, B., Kibler, B. & Millot, G. Collision of Akhmediev breathers in nonlinear fiber optics. *Phys. Rev. X* **3**, 041032 (2013).

51. Soto-Crespo, J. M., Devine, N. & Akhmediev, N. Integrable turbulence and rogue waves: breathers or solitons? *Phys. Rev. Lett.* **116**, 103901 (2016).

52. Meng, F. et al. Intracavity incoherent supercontinuum dynamics and rogue waves in a broadband dissipative soliton laser. *Nat. Commun.* **12**, 5567 (2021).

53. Gemmrich, J. & Cicon, L. Generation mechanism and prediction of an observed extreme rogue wave. *Sci. Rep.* **12**, 1718 (2022).

54. Arecchi, F. T., Bortolozzo, U., Montina, A. & Residori, S. Granularity and inhomogeneity are the joint generators of optical rogue waves. *Phys. Rev. Lett.* **106**, 153901 (2011).

55. Leonetti, M. & Conti, C. Observation of three dimensional optical rogue waves through obstacles. *Appl. Phys. Lett.* **106**, 254103 (2015).

56. Akhmediev, N., Ankiewicz, A. & Soto-Crespo, J. M. Rogue waves and rational solutions of the nonlinear Schrödinger equation. *Phys. Rev. E* **80**, 026601 (2009).

57. Kang, J. U., Stegeman, G. I., Aitchison, J. S. & Akhmediev, N. Observation of manakov spatial solitons in AlGaAs planar waveguides. *Phys. Rev. Lett.* **76**, 3699–3702 (1996).

58. Barad, Y. & Silberberg, Y. Polarization evolution and polarization instability of solitons in a birefringent optical fiber. *Phys. Rev. Lett.* **78**, 3290–3293 (1997).

59. Cundiff, S. T. et al. Observation of polarization-locked vector solitons in an optical fiber. *Phys. Rev. Lett.* **82**, 3988–3991 (1999).

60. Akhmediev, N., Królikowski, W. & Snyder, A. W. Partially coherent solitons of variable shape. *Phys. Rev. Lett.* **81**, 4632–4635 (1998).

61. Kanna, T. & Lakshmanan, M. Exact soliton solutions, shape changing collisions, and partially coherent solitons in coupled nonlinear Schrödinger equations. *Phys. Rev. Lett.* **86**, 5043–5046 (2001).

62. Soljačić, M. et al. Collisions of two solitons in an arbitrary number of coupled nonlinear Schrödinger equations. *Phys. Rev. Lett.* **90**, 254102 (2003).

63. Chen, S., Soto-Crespo, J. M. & Grelu, P. Coexisting rogue waves within the (2+1)-component long-wave–short-wave resonance. *Phys. Rev. E* **90**, 033203 (2014).

64. Kodama, Y. & Hasegawa, A. Nonlinear pulse propagation in a monomode dielectric guide. *IEEE J. Quantum Electron.* **23**, 510–524 (1987).

65. Agrawal, G. P. Nonlinear Fiber Optics, 4th ed. (Academic, San Diego, 2007).

66. Moses, J. & Wise, F. W. Controllable self-steepening of ultrashort pulses in quadratic nonlinear media. *Phys. Rev. Lett.* **97**, 073903 (2006).

67. Baronio, F. et al. Spectral shift of femtosecond pulses in nonlinear quadratic PPSLT crystals. *Opt. Express* **14**, 4774–4779 (2006).

68. Moses, J., Malomed, B. A. & Wise, F. W. Self-steepening of ultrashort optical pulses without self-phase-modulation. *Phys. Rev. A* **76**, 021802(R) (2007).

69. Chan, H. N., Chow, K. W., Kedziora, D. J., Grimshaw, R. H. J. & Ding, E. Rogue wave modes for a derivative nonlinear Schrödinger model. *Phys. Rev. E* **89**, 032914 (2014).

70. Chen, S., Baronio, F., Soto-Crespo, J. M., Liu, Y. & Grelu, P. Chirped Peregrine solitons in a class of cubic-quintic nonlinear Schrödinger equations. *Phys. Rev. E* **93**, 062202 (2016).

71. Chen, S. et al. Super chirped rogue waves in optical fibers. *Opt. Express* **27**, 11370–11384 (2019).

72. Yeh, C. & Bergman, L. Enhanced pulse compression in a nonlinear fiber by a wavelength division multiplexed optical pulse. *Phys. Rev. E* **57**, 2398–2404 (1998).

73. Matthews, M. R. et al. Vortices in a Bose-Einstein Condensate. *Phys. Rev. Lett.* **83**, 2498–2501 (1999).

74. Scott, A. C. Launching a Davydov soliton: I. soliton analysis. *Phys. Scr.* **29**, 279–283 (1984).

75. Tsuchida, T. & Wadati, M. New integrable systems of derivative nonlinear Schrödinger equations with multiple components. *Phys. Lett. A* **257**, 53–64 (1999).

76. Ling, L., Zhao, L.-C & Guo, B. Darboux transformation and multi-dark soliton for *N*-component nonlinear Schrödinger equations. *Nonlinearity* **28**, 3243–3261 (2015).

77. Ye, Y., Zhou, Y., Chen, S., Baronio, F. & Grelu, P. General rogue wave solutions of the coupled Fokas-Lenells equations and non-recursive Darboux transformation. *Proc. R. Soc. A* **475**, 20180806 (2019).

78. Yang, B. & Yang, J. Universal rogue wave patterns associated with the Yablonskii–Vorob'ev polynomial hierarchy. *Phys. D.* **425**, 132958 (2021).

79. Kleefeld, B., Khaliq, A. Q. M. & Wade, B. A. An ETD Crank-Nicolson method for reaction-diffusion systems. *Numer. Methods PDEs* **28**, 1309–1335 (2012).

80. Chen, S. et al. Optical Peregrine rogue waves of self-induced transparency in a resonant erbium-doped fiber. *Opt. Express* **25**, 29687–29698 (2017).

81. Kaup, D. J., Reiman, A. & Bers, A. Space-time evolution of nonlinear three-wave interactions. I. Interaction in a homogeneous medium. *Rev. Mod. Phys.* **51**, 275–309 (1979).

82. Baronio, F., Conforti, M., Degasperis, A. & Lombardo, S. Rogue waves emerging from the resonant interaction of three waves. *Phys. Rev. Lett.* **111**, 114101 (2013).

83. Chen, S. et al. Optical rogue waves in parametric three-wave mixing and coherent stimulated scattering. *Phys. Rev. A* **92**, 033847 (2015).

84. Yang, B. & Yang, J. General rogue waves in the three-wave resonant interaction systems. *IMA J. Appl. Math.* **86**, 378–425 (2021).

Author contributions

S.C. conceived the work; S.C., L.B., C.P. and C.H. did the theoretical derivation; S.C. and F.B. performed numerical calculations and simulations; S.C., F.B., P.G. and N.A. wrote the manuscript. All the authors contributed to the discussions of the results and the manuscript preparation.

Competing interests

The authors declare no competing interests.

Additional information

Supplementary information The online version contains supplementary material available at https://doi.org/10.1038/s42005-022-01076-x.

Correspondence and requests for materials should be addressed to Shihua Chen, Fabio Baronio, Philippe Grelu or Nail Akhmediev.

Peer review information *Communications Physics* thanks the anonymous reviewers for their contribution to the peer review of this work. Peer reviewer reports are available.

Reprints and permission information is available at http://www.nature.com/reprints

Publisher's note Springer Nature remains neutral with regard to jurisdictional claims in published maps and institutional affiliations.